Time-reversal symmetry breaking in frustrated superconductor Re₂Hf

Manasi Mandal,[1] Anshu Kataria,[1] Chandan Patra,[1] D. Singh,[2] P. K. Biswas,[2] A. D. Hillier,[2]
Tanmoy Das,[3,*] and R. P. Singh ![ORCID][1,†]

[1]*Department of Physics, Indian Institute of Science Education and Research Bhopal, Bhopal 462066, India*
[2]*ISIS Facility, STFC Rutherford Appleton Laboratory, Harwell Science and Innovation Campus, Oxfordshire OX11 0QX, United Kingdom*
[3]*Department of Physics, Indian Institute of Science, Bangalore 560012, India*

Geometrical frustration leads to novel quantum phenomena such as the spin-liquid phase in triangular and kagome lattices. Intraband and interband Fermi surface (FS) nesting can drive unique superconducting (SC) ground states with d-wave and $s^{\pm}$-pairing symmetries, respectively, according to the criterion that the SC gap changes sign across the nesting wave vector. For an odd number of FSs, when multiple interband nesting is of comparable strength, the sign-reversal criterion between different FS sheets can lead to frustration, which promotes novel SC order parameters. Here, we report the experimental observation of a time-reversal symmetry breaking pairing state in Re₂Hf resulting from FS nesting frustration. Furthermore, our electronic specific heat and transverse-field muon spin rotation experiments suggest a fully gapped pairing symmetry. The first-principles electronic structure calculation reveals multiple Fermi surface sheets with comparable interband nesting strength. Implementing the *ab initio* band structure, we compute spin-fluctuation mediated SC pairing symmetry which reveals an $s + is'$-pairing state—consistent with experimental observations. Our investigation demonstrates an alternative SC state which provides a putative setting for both applied and fundamental study.

I. INTRODUCTION

Conventional superconductivity is mediated by electron-phonon coupling, which induces an attractive interaction that results in a unique ground state of isotropic and fixed-sign pairing symmetry. The attractive interaction leaves little room for exotic pairing symmetries. On the other hand, while unconventional superconductivity is yet to be fully understood, the possibility of having novel and exotic pairing symmetries due to the interplay of structural symmetries and Fermi surface (FS) topology make it an attractive topic of research [1].

The theory of spin-fluctuation mediated unconventional superconductivity requires a pairing symmetry that must change sign across the Fermi surfaces (FSs) related to the nesting wave vector [2–13]. In a single FS sheet, if the pairing symmetry changes sign between different parts of the same FS, it must go through a zero gap state. This gives rise to nodal superconductivity (SC), for example, d-wave gap symmetry in cuprates [2–10], in some of the heavy fermions [11,14–16], and other compounds [12,13,17]. In a multiband SC, if the FS nesting occurs between different FS sheets, the SC gap may possess an opposite sign between different FS sheets but a single sign on a single FS sheet. Such solutions lead to the $s^{\pm}$-pairing state, which is fully gapped (nodeless), as seen in pnictides [18–21] and proposed in some other systems [14,22]. It is interesting to ask what happens when there exists an odd number of FS sheets (say three), and the pairing interaction promotes an interband sign-reversal

pairing symmetry. How do we fix the sign of the gap on the third FS sheet, as schematically shown in Fig. 1. For example, when the three interband FS nestings are of comparable strengths and promote an interband $s^{\pm}$-pairing state, any two FSs possess opposite SC gaps, while the third FS has the equal probability of having $\pm$SC gap. In such a frustrated SC phase, the lowest ground state can be a superposition state of both gaps, which gives a time-reversal breaking $s \pm is$-pairing state. So far, time-reversal symmetry breaking (TRSB) superconductivity have been reported in a very few materials, e.g., Sr₂RuO₄ [23,24] and (U, Th)Be₁₃ [25–28], (Pr, La)(Ru, Os)₄Sb₁₂ [29,30], PrPt₄Ge₁₂ [31], LaNiGa₂ [32], UPt₃ [33], Lu₅Rh₆Sn₁₈ [34], Re₆X [35–38], LaNiC₂ [39], La₇(Ir/Rh)₃ [40,41], and very recently in Sr$_x$Bi₂Se₃ [42],4Hb-TaS₂ [43], and Ba$_{1-x}$K$_x$Fe₂As₂ [44]. In these materials, the TRSB superconductivity is often stabilized by mainly ferromagnetic fluctuations or spin-orbit coupling (SOC).

In this paper, we report the evidence of a TRSB SC ground state resulting from a mechanism of FS nesting frustrations in Re₂Hf. This constitutes an experimental observation of multiband superconductivity exhibiting frustration.

II. NORMAL AND SUPERCONDUCTING STATE PROPERTIES

Re-based binary compounds (Re-X) form in centrosymmetric and noncentrosymmetric crystal structures depending on the Re/X stoichiometry ratio and most of these binary compounds are superconductors. Re₂Hf is another member of this family, forming a C_{14} Laves phase with a centrosymmetric crystal structure. A hexagonal C_{14}-type Laves phase is a form

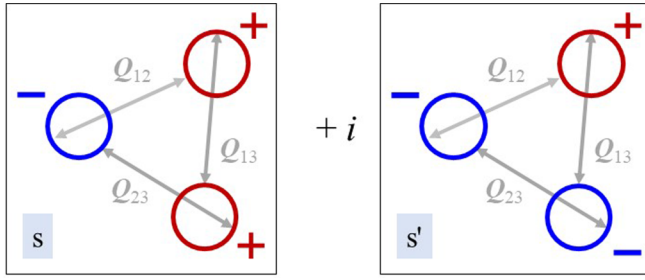*tnmydas@iisc.ac.in
†rpsingh@iiserb.ac.in

FIG. 1. A schematic demonstration of frustrated pairing symmetry in a three FSs (circles). Blue and red colors denote different signs of the SC gap. Q_{ij} are the assumed interband nesting vectors between the ith and jth FS sheets, with comparable nesting strength. Each nesting promotes a sign reversal of the SC gap between nested FSs, hence two degenerate s and s' pairing symmetries arise. The ground state is the linear superposition of the two solutions, which is an $s + is$-pairing symmetry.

of well-known Laves phases with the general composition of AB_2, and the B atoms often dominate the electronic properties of the Laves phases [45]. The Re$_2$Hf sample was prepared via the standard arc melting method. We characterized the compound by magnetization, resistivity, and specific heat measurements. The details of sample preparation and experimental techniques are given in the Supplemental Material [46]. These measurements confirm that Re$_2$Hf is a type-II superconductor with $T_C^{\mathrm{mag}} = 5.7(1)$ K [Fig. 2(a)]. Zero resistivity further confirms the superconductivity of the alloy [inset of Fig. 2(a)].

We estimated the lower critical field $H_{C1}(0)$ from the low-field magnetization curves $M(H)$ in the range of 0–30 mT taken at different temperatures as shown in the inset of Fig. 2(b). $H_{C1}(0)$ was estimated to be 12.7(1) mT by fitting the data in accordance with the Ginzburg-Landau (GL) equation $H_{C1}(T) = H_{C1}(0)[1 - (\frac{T}{T_C})^2]$. Magnetization measurements were done in different magnetic fields up to 1.0 T to calculate the second-order transition field $H_{C2}(0)$, as shown

in the inset of Fig. 2(c). Since, in the case of a type-II material, the magnetic field can penetrate the sample and reduce the gap function, T_C shifts to lower temperature with the increment of the applied field. Data were well fitted in the low-field region by using the GL formula $H_{C2}(T) = H_{C2}(0)\frac{(1-t^2)}{(1+t^2)}$, where $t = T/T_C$. In the high-field region, a concave nature of $H_{C2}(T)$ was observed in magnetization measurements. A similar behavior of $H_{C2}(T)$ was noted when calculated from specific heat and resistivity measurements. The data were well fitted with the two-gap model [47]. The dashed line gives a two-gap fit of the data in the whole region, indicating the possible multiband superconductivity in Re$_2$Hf compound. The estimated value of $H_{C2}^{\mathrm{mag}}(0)$ is 1.17(2) T. We calculated the Ginzburg-Landau coherence length $\xi_{\mathrm{GL}}(0) \simeq 167$ Å from the relation $H_{C2}(0) = \frac{\Phi_0}{2\pi\xi_{\mathrm{GL}}^2}$, where Φ_0 (= 2.07 × 10^{-15} T m^2) is the magnetic flux quantum [48]. Since a Cooper pair breaks due to the applied magnetic field, more precise treatment of the second-order transition field $H_{C2}(0)$, including the Pauli paramagnetic and orbital diamagnetic effects together, has been given by Maki [49] in the limit of a very short mean free path. The Maki parameter α_M is the measure of the relative strengths of the orbital and Pauli limiting values of H_{C2} and is given by $\alpha_M = \sqrt{2}H_{C2}^{\mathrm{orbital}}(0)/H_{C2}^p(0)$. For BCS superconductors in the dirty limit, the orbital limit of the upper critical field $H_{C2}^{\mathrm{orbital}}(0)$ can be calculated by the Werthamer-Helfand-Hohenberg (WHH) [50,51] expression $H_{C2}^{\mathrm{orbital}}(0) = -\alpha T_C \frac{dH_{C2}(T)}{dT}|_{T=T_C}$, where α is the purity factor for dirty limit (= 0.693) superconductors and the initial slope $\frac{-dH_{C2}(T)}{dT}|_{T=T_C}$ was calculated from the H_{C2} -T phase diagram. The obtained vale of $H_{C2}^{\mathrm{orbital}}(0)$ is 0.73 T. The obtained value of $\alpha_M = 0.10$ for Re$_2$Hf indicates that the effect of the Pauli limiting field is negligible in the breaking of Cooper pairs. The penetration depth $\lambda_{\mathrm{GL}}(0)$ and GL parameter k_{GL} were estimated as 1742 Å and 10.38, respectively, for Re$_2$Hf by using relations (1) and (2):

$$H_{C1}(0) = \frac{\Phi_0}{4\pi\lambda_{\mathrm{GL}}^2(0)}\left(\ln\frac{\lambda_{\mathrm{GL}}(0)}{\xi_{\mathrm{GL}}(0)} + 0.497\right), \qquad (1)$$
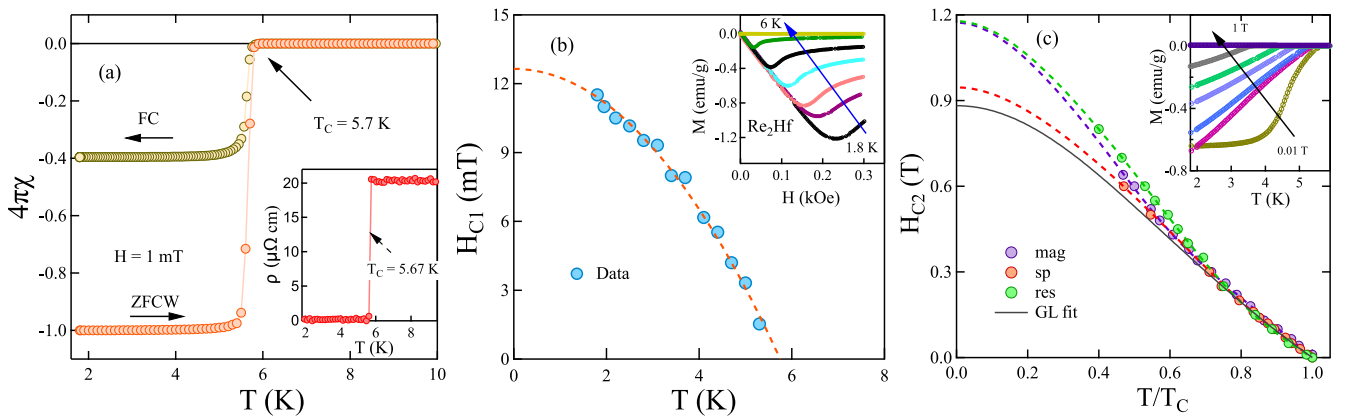

FIG. 2. (a) The temperature dependence of the magnetic susceptibility at 1 mT applied field. The inset shows the zero resistivity. (b) Temperature dependence of the lower critical field H_{C1} was fitted using the Ginzburg-Landau relation. (c) $H_{C2}(0)$ was calculated via magnetization, resistivity, and heat capacity measurements. The dotted lines are two-gap fittings of the data. The inset shows the $M(T)$ curves for various applied magnetic fields.
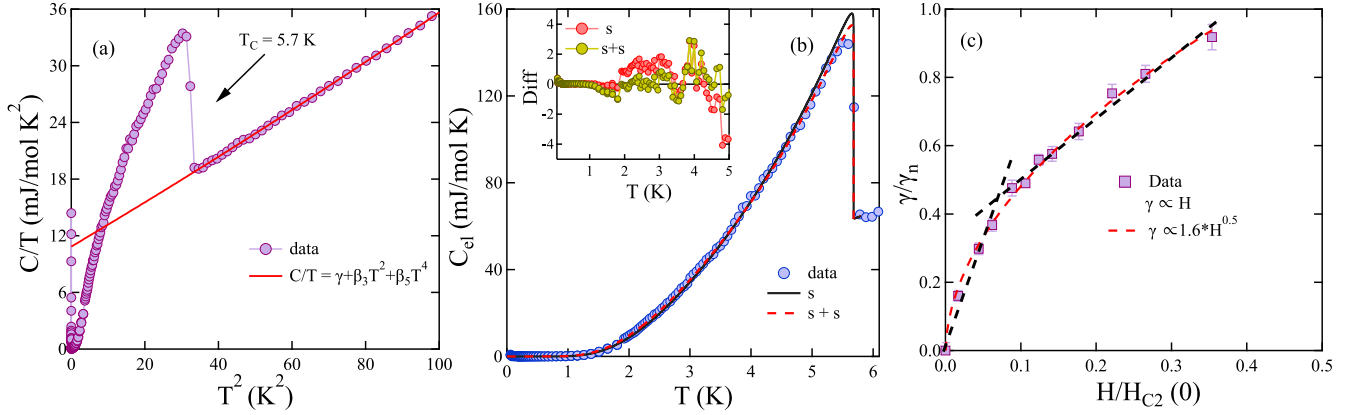
FIG. 3. (a) Normal-state fitting of specific heat data at $H = 0$. (b) The temperature dependence of the electronic specific heat C_{el} in the superconducting state fitted with the α model. The inset shows the difference between the observed data and the theoretical model. (c) γ and H were plotted vs each other after normalizing by γ_n and $H_{C2}(0)$.

and

$$k_{GL} = \frac{\lambda_{GL}(0)}{\xi_{GL}(0)}. \qquad (2)$$

The GL parameter $k_{GL} \gg \frac{1}{\sqrt{2}}$, indicating that Re$_2$Hf is a type-II superconductor. The thermodynamic critical field H_C is obtained around 0.08 T from the relation $H_{C1}(0)H_{C2}(0) = H_C^2 \ln k_{GL}$.

The exact SC gap nature is investigated using specific heat measurements. Heat capacity measurements were performed at zero fields as well as at different fields to analyze the phonon properties and electronic density of states of the sample. The superconducting transition, which is manifested by a pronounced jump in the heat capacity data, is observed at 5.70 K [Fig. 3(a)]. We analyzed the low-temperature normal-state specific heat data by using the relation $\frac{C}{T} = \gamma_n + \beta_3 T^2 + \beta_5 T^4$, where γ_n is the Sommerfeld coefficient, β_3 is the Debye constant, and β_5 is the anharmonic contribution to the specific heat. The extrapolation of normal state behavior below T_C, to the $T \to 0$ limit, allows for the determination of normal-state coefficients. From the β_3 (=0.23) values obtained experimentally, we calculated the Debye temperatures θ_D of the compounds using the formula $\theta_D = (\frac{12\pi^4 RN}{5\beta_3})^{\frac{1}{3}}$, where N (=3) is the number of atoms per formula unit, and R is the molar gas constant (=8.314 J mol^{-1} K^{-1}), which was based on the simple Debye model for the phonon contribution to the specific heat. The estimated θ_D value was 294 K. For noninteracting fermions, the Sommerfeld coefficient γ_n is proportional to the density of states $D_C(E_F)$ at the Fermi level which was calculated to be 4.71 states/(eV f.u.) from the relation $\gamma_n = (\frac{\pi^2 k_B^2}{3})D_C(E_F)$, where $k_B \simeq 1.38 \times 10^{-23}$ J K^{-1}. The strength of the attractive interaction between the electron and phonon can be estimated by the electron-phonon coupling constant $\lambda_{e\text{-ph}}$ in the McMillan equation [52] $\lambda_{e\text{-ph}} = \frac{1.04 + \mu^* \ln(\theta_D/1.45 T_C)}{(1 - 0.62\mu^*)\ln(\theta_D/1.45 T_C) - 1.04}$, where μ^* (=0.13 for many intermetallic superconductors) is the repulsive screened Coulomb parameter. The calculated value of $\lambda_{e\text{-ph}} = 0.67$ represents Re$_2$Hf as a moderately coupled superconductor [53,54].

The electronic contribution to the specific heat in the superconducting state C_{el} can be calculated by subtracting the phononic contribution from the measured data C by the relation $C_{el} = C - \beta_3 T^3 - \beta_5 T^5$. The electronic contribution to the specific heat was fitted using the α model [55] (detailed in the Supplemental Material [46]). The data were well fitted with both s and $s + s$ waves but two-gap models though the $s + s$ model yield a better goodness of fit (χ^2) compared to the s model fit as shown in Fig. 3(b). In the case of the $s + s$ model fit the values of the energy gap $\frac{\Delta(0)}{k_B T_C}$ are 1.85 and 1.60 with a weight factor of the second gap of 0.43. It is visible that the $s + s$ model fits better over the whole temperature range than the s models. The inset of Fig. 3(b) shows the difference between the observed data and the theoretical model. The systematic deviation of the s and $s + s$ models from the experimental data may suggest the effect from the polycrystalline nature of the sample. But the deviation amplitude denotes the goodness of fit that shows the $s + s$ model with a significant fraction of the second gap best fits the experimental results. The good agreement of the $s + s$ model with observed data indicates the presence of multiple nodeless gaps on the FS. To quantitatively analyze the T dependence of the electronic contribution of the specific heat, the Sommerfeld coefficient γ was calculated by fitting the C_{el}/T vs T data with the equation $\frac{C_{el}}{T} = \gamma + \frac{A}{T} \exp(\frac{-b T_C}{T})$ for each field [56]. The field dependence of the Sommerfeld coefficient γ is shown in Fig. 3(c), where γ and H are normalized by γ_n (=11.1 mJ mol^{-1} K^{-2}) and $H_{C2}(0)$ (=1.17 T), respectively. Here, we can observe γ increases linearly with H in the lower-field region up to a crossover field $H^* \simeq 0.07 H_{C2}(0)$, which is slightly less than the theoretical value $0.3 H_{C2}(0)$ expected for the completely isotropic gap case [56,57]. In the framework of the theory proposed by Nakai *et al.* [57], γ is proportional to the number of field-induced vortices, i.e., $\gamma \propto H$ for a fully gapped superconductivity whereas a nonlinear behavior $\gamma \propto H^{0.5}$ is predicted for a highly anisotropic gap or a gap with nodes. At higher fields, interactions between the vortices result in the delocalization of quasiparticles, leading to a nonlinear increase in γ, and the crossover field reduces with the degree of the gap anisotropy [58]. The data were well fitted
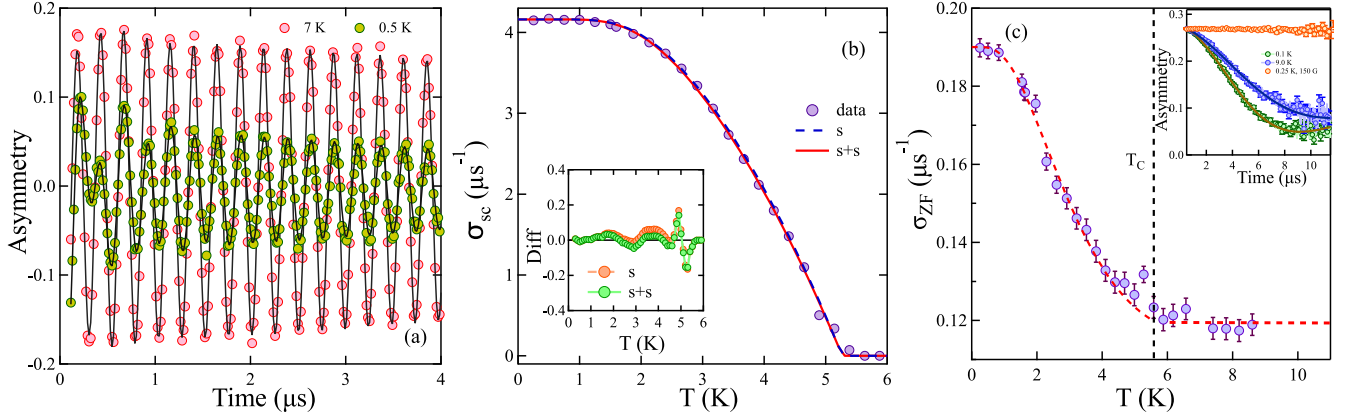
FIG. 4. (a) TF-μSR asymmetry spectra collected above ($T = 7$ K) and below ($T = 0.5$ K) the transition temperature T_C at $H = 30$ mT where solid lines represent the fit to the data using Eq. (3). (b) The temperature dependence of σ_{sc} is fitted with different models. The inset shows the difference between the experimental results and theoretical model. (c) Temperature dependence of σ_{ZF} and the inset shows the time evolution of the spin polarization of muons under zero-field conditions.

with $\gamma \propto 1.6H^{0.5}$, indicating a possible unconventional superconducting energy gap. The black dashed line guides the eye to two linear fits with different slopes, which can correspond to the two isotropic gaps on the FSs. A similar behavior of the Sommerfield coefficient was observed for popular multigap superconductors such as MgB$_2$ [59,60] and 2H-NbSe$_2$ [61]. Such a nontrivial nature of γ suggests the presence of an unconventional single-particle energy gap, as predicted by the theoretical results [56,57].

III. MUON SPIN ROTATION AND RELAXATION MEASUREMENTS

The gap structure of the SC state is further probed by the transverse-field muon spin rotation (TF-μSR) measurements. Figure 4(a) shows the TF-μSR precessional signals for Re$_2$Hf collected above and below T_C. The normal-state spectra show a homogeneous field distribution throughout the sample, with a weak depolarization arising from the dipolar nuclear field. In contrast, the SC state spectra show a strong depolarization, indicating the formation of an inhomogeneous field distribution in the flux line lattice (FLL) state. The decaying multicomponent Gaussian oscillatory function best fitted the time domain of the transverse-field μSR spectra with an oscillatory background term that emerges from the muons implanted directly into the silver sample holder that does not depolarize,

$$G_{TF}(t) = \sum_{i=1}^{N} A_i \exp\left(\frac{-\sigma_i^2 t^2}{2}\right) \cos(\gamma_\mu B_i t + \phi)$$
$$+ A_{bg} \cos(\gamma_\mu B_{bg} t + \phi), \tag{3}$$

where ϕ, A_i, B_i, σ_i, and $\gamma_\mu/2\pi = 135.5$ MHz/T are the initial phase of the initial muon spin polarization with respect to the positron detector, asymmetry, mean field (first moment) of the ith component of the Gaussian distribution, relaxation rate, and muon gyromagnetic ratio, respectively. A_{bg} and B_{bg} are the background contributions for the asymmetry and the field, respectively. The terms mainly arise from the muons that miss the sample and hit the sample holder or the cryostat walls. The

temperature dependence of effective depolarization rate σ was calculated by the second moment method where the first and second moments are described as

$$\langle B \rangle = \sum_{i=1}^{N} \frac{A_i B_i}{A_1 + A_2 + \cdots + A_N}, \tag{4}$$

$$\langle \Delta B^2 \rangle = \sum_{i=1}^{N} \frac{A_i[(\sigma_i/\gamma_\mu)^2 + (B_i - \langle B \rangle)^2]}{A_1 + A_2 + \cdots + A_N} = \frac{\sigma^2}{\gamma_\mu^2}. \tag{5}$$

The asymmetry spectra were fitted with three Gaussian components to maintain the quality of fit such that χ^2 (normalized to the degrees of freedom) is close to 1. σ is the incorporate of depolarization arising due to nuclear dipolar moments (σ_N) and the field variation across the flux line lattice (σ_{sc}) by the quadratic relation $\sigma^2 = \sigma_{sc}^2 + \sigma_N^2$. We have extracted σ_{sc} from the above relation. The temperature dependence of the depolarization arising due to the field variation across the flux line lattice (σ_{sc}) is displayed in Fig. 4(b). The inset of Fig. 4(b) shows the difference between the experimental results and the theoretical model. The temperature dependence of σ_{sc} is seen nearly constant below $\simeq T_C/3$, indicating the absence of nodes in the SC energy gap at the FS. We have fitted the data with different models, while only a two-gap scenario with both gaps being nodeless gives good fitting over most regions. The details of the fitting functions are summarized in the Supplemental Material [46]. This suggests the dominating s-wave behavior in the compounds with an isotropic or nearly isotropic gap in the electronic density of states at the Fermi level. The two-gap model yields a value of the BCS ratio $\frac{\Delta(0)}{k_B T_C}$ as 1.89 and 1.82 with a weighting factor 0.21 to the second gap. While both single- and two-gap s-wave models yield good agreement, the two-gap fitting covers the whole temperature region with a better goodness of fit. The gap values are slightly higher than those estimated from specific heat values due to the applied field during measurement. The calculated value of $\frac{\Delta(0)}{k_B T_C}$ is higher than the BCS predicted value of 1.76, indicating deviations from the weak coupling BCS pairing scenario. The fitting with the local London approximation in the clean limit yields $\lambda(0) = 1397(10)$ Å.

To further investigate the occurrence of TRS breaking in Re$_2$Hf, a systematic zero-field (ZF) μSR was performed at different temperatures. The inset of Fig. 4(c) shows the ZF-μSR spin relaxation spectra, where there is an apparent change in the relaxation behavior of the spectra recorded above ($T = 9$ K) and below ($T = 0.1$ K) T_C. This indicates the presence of spontaneous magnetic fields in the SC state. We have fitted ZF-μSR data by a damped Gaussian Kubo-Toyabe (KT) function [62] with a background contribution associated with the muon stopping in the silver sample holder. The damped Gaussian Kubo-Toyabe (KT) function is given by

$$G(t) = A_1 \exp(-\Lambda t)G_{\text{KT}}(t) + A_{\text{bg}}, \qquad (6)$$

with

$$G_{\text{KT}}(t) = \frac{1}{3} + \frac{2}{3}\big(1 - \sigma_{\text{ZF}}^2 t^2\big) \exp\left(\frac{-\sigma_{\text{ZF}}^2 t^2}{2}\right), \qquad (7)$$

where A_1 is the initial sample asymmetry, and σ_{ZF} and Λ are the Gaussian and an additional relaxation rate, respectively. The temperature dependence of the Gaussian relaxation rate σ_{ZF} is shown Fig. 4(c). σ_{ZF} gradually increases below the superconducting transition temperature (the dotted line guides the eye), indicating a possible TRS breaking signal. We have also performed longitudinal-field (LF)-μSR measurements at 0.25 K of 15 mT, shown by the orange flat asymmetry spectra in Fig. 4(c). The applied field decouples the static internal field, excluding the possibility of an impurity-induced relaxation. The calculated value of the spontaneous field B_{int} in the SC region is 0.116 mT. The appearance of such spontaneous fields in the SC state provides strong evidence for a TRS broken pairing state. The internal field value is highest among all the TRS breaking superconductors, suggesting a distinctive SC state in this compound.

IV. ELECTRONIC PROPERTIES

From the general physics of the Laves phase elements as is Re$_2$Hf, it is expected that the electronic structure of Re plays a crucial role in superconductivity [45,63]. Re$_2$Hf belongs to the $P6_3/mmc$ space group (No. 194) and has the hexagonal point group of D_{6h}. We compute the electronic structure using the Vienna *ab initio* simulation package (VASP) [64], and the Perdew-Burke-Ernzerhof (PBE) form for the exchange-correlation functional [65]. The lattice parameters are allowed to relax, and the values are found to be $a = 5.29$ Å, and $c/a = 1.63$, close to the experimental value [66]. To deal with the strong correlation effect of the d electrons of Re atoms, we employed the local density approximation plus Hubbard U (LDA+U) method with a standard database value of $U = 2.4$ eV. The spin-polarized calculation is performed to confirm that the material is nonmagnetic. Finally, the calculations are repeated with and without the spin-orbit coupling.

There are five FS sheets, as shown in Fig. 5(a) for the SOC split bands. All FSs show substantial three-dimensional behavior. Among all the FSs, FS 4 has the largest area and then FS 3 and so on. For all bands, we find intraband FS nesting is much weaker than the interband components, and expectedly, the FS nesting strength between FS 4 and others is stronger while those among the other FSs are equivalent, causing frustrations in the nesting profile [see Fig. 5(b)]. Without SOC,
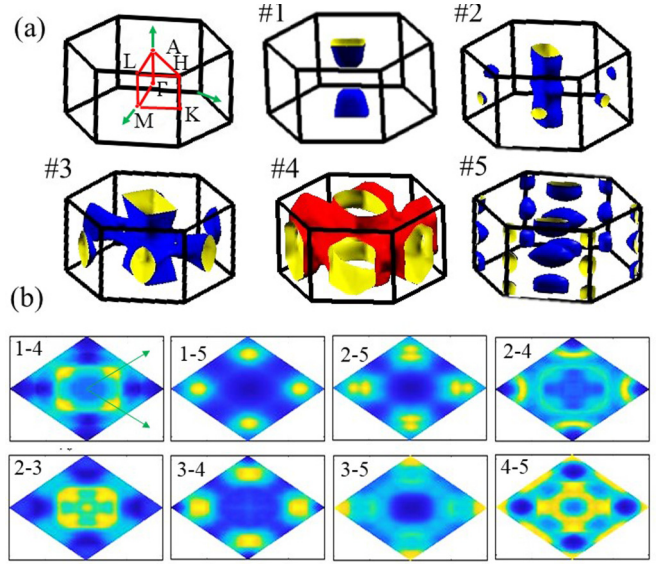

FIG. 5. Theoretical results of the FS topology and FS nestings. (a) Computed FS topologies for different bands in the first Brillouin zones for calculations with SOC. The blue and red color on the FSs denote the sign of the computed pairing symmetry, while the yellow color is for visualization. (b) Computed static bare susceptibilities are shown for several representative interband components, which are dominant in this material. The blue to yellow color denotes the minimum to the maximum value of the susceptibility.

the topology of the FSs remains similar, but two additional small FSs appear. The following calculations of the SC pairing symmetry are repeated for the SOC-free band structures, and the results of the $s + is'$-pairing symmetry are found to be robust.

V. SPIN-FLUCTUATION MEDIATED SUPERCONDUCTIVITY

We consider a multiband Hubbard model with intra- and interband on-site interactions U and V, respectively. The density-density fluctuation mediated pairing interaction $\Gamma(\mathbf{q})$ is obtained within the random phase approximation (RPA) by summing the so-called bubble and ladder diagrams [2,7,11,18], and the result is

$$\Gamma(\mathbf{q}) = \tfrac{1}{2}[3U_s\chi_s(\mathbf{q})U_s - U_c\chi_c(\mathbf{q})U_c + U_s + U_c]. \qquad (8)$$

The subscripts s and c denote spin and charge fluctuation channels, respectively. $U_{s/c}$ are the on-site interaction tensors for spin and charge fluctuations, respectively, whose diagonal terms involve intraband Hubbard U and the off-diagonal components give the interband Hubbard V. $\chi_{s/c}$ are the RPA spin and charge susceptibilities computed by directly including the density functional theory (DFT) band structures. The details of the formalism are given in the Supplemental Material [46].

We compute the eigenvalue and eigenfunctions of the pairing interaction $\Gamma(\mathbf{q} = \mathbf{k} - \mathbf{k}')$ on the three-dimensional (3D) FS by solving the following equation:

$$\Delta(\mathbf{k}) = -\lambda \sum_{\mathbf{k}'} \Gamma(\mathbf{k} - \mathbf{k}')\Delta(\mathbf{k}'). \qquad (9)$$

$\Delta(\mathbf{k})$ is an N-component eigenvector at each $\mathbf{k}$, denoted by $\Delta(\mathbf{k}) = \{\Delta_i(\mathbf{k})\}$, where $i = 1 - N$ with N being the total number of bands. To consider the intra- and interband nestings on equal footings, we construct a pairing potential matrix $\mathbf{\Gamma}$ of dimension $N' \times N'$, where $N' = N \times N_k$ with N_k being the total number of coarse-grained Brillouin zone k points. λ is the overall pairing eigenvalue (proportional to the SC coupling strength). Since the pairing potential is repulsive here, the highest *positive* eigenvalue λ, and the corresponding pairing symmetry can be shown to govern the lowest free-energy value in the SC state [7].

We numerically solve Eq. (9), and find several (nearly) degenerate solutions. We present one of the solutions by projecting the eigenstate $\Delta(\mathbf{k})$ onto different band bases $\delta_i(\mathbf{k})$ in Fig. 5(a) by the blue to red color (positive to negative value of the SC gap) on the FSs. We make several important observations. (i) All the degenerate gap solutions yield a negative gap on FS 4, while the sign of the gap is frustrated among the remaining four FSs. This is consistent with the fact that FS 4 has the largest volume and has comparable interband nestings with all other FSs. Therefore, the SC solution is favored for a sign reversal in all other bands with respect to FS 4. (ii) The other nesting channels have variable strength and nesting wave vectors. Several dominant (static) spin-fluctuation profiles are shown in Fig. 5(b). We observe that there are several interband nesting profiles which are nearly degenerate. For example, the nestings between FSs 2–4 are very much degenerate than that between FSs 3 and 4, 1–5, and 2–5. Therefore, for the negative gap in FS 4, the FS 1–5 and FS 2–5 nestings frustrate the sign on the FS 5 with respect to FS 1 and FS 2. Similarly, the similar nesting profiles between bands 1–4, 2 and 3, and 4 and 5 tend to frustrate the SC gap's sign between FS 1 and FS 5. (iii) In all cases, we find that the intraband FS nesting strength is considerably small. This plays a key role in the absence of any $\mathbf{k}$-space anisotropy of the gap within a given band.

VI. DISCUSSION OF THE SC GAP SYMMETRY

The origin of the TRS breaking complex pairing eigenstate is understood as follows. We express the gap functions as $\Delta_i(\mathbf{k}) = \eta_i g_i(\mathbf{k})$, where η_i is the gap value and $g_i(\mathbf{k})$ incorporates the $\mathbf{k}$-space anisotropy, and i is the band index. The sign reversal of the gaps can now occur either in η_i between different bands $\mathrm{sgn}[\eta_i] \neq \mathrm{sgn}[\eta_{j \neq i}]$, and/or $\mathrm{sgn}[g_i(\mathbf{k})] \neq \mathrm{sgn}[g_j(\mathbf{k} + \mathbf{q})]$ for $i = j$ (intraband) or $i \neq j$ (interband), where $\mathbf{q}$ is the nesting vector. The hexagonal group $D_{6h} \otimes T$, where T is the time-reversal symmetry, is split into the A_{1g} and E_{2g} irreducible representations [67]. This implies that $g_i(\mathbf{k})$ can have s-wave or d-wave symmetries.

(i) In the limit when the interband interactions are much smaller than the intraband components, Eq. (9) decouples to N-separate eigenvalue equations in the momentum space. Given that $\lambda > 0$, and $\Gamma > 0$, the only allowed solutions of Eq. (9) are those for which each $g_i(\mathbf{k})$ component changes sign across the corresponding nesting vector. This means $g(\mathbf{k}) \in E_{2g}$. There is little possibility in this case to obtain any other exotic order parameter such as a TRSB complex order parameter.

(ii) In the other limit of $\Gamma_{i \neq j, j} \gg \Gamma_{ii}$, generally both A_{1g} and E_{2g} symmetries may arise: A_{1g} is preferable when the sign reversal occurs in η_i between two bands due to interband nesting without a preferential wave vector or if there are multiple nestings of comparable strengths causing frustration (our case). This gives an $s^{\pm}$-pairing symmetry. E_{2g} symmetry can arise here when the interband nesting promotes a sign reversal in both η_i and $g_i(\mathbf{k})$. In both cases, one may obtain a TRSB combination such as an $s + is$ or $d + id$ for the reasons discussed below.

(iii) In the intermediate region where both intraband and interband nestings are comparable, both A_{1g} and E_{2g} symmetries are allowed, and since these two irreducible representations do not mix, a stable solution would require a TRSB combination, i.e., an $s + id$ order parameter. Our numerical simulation predicts an $s + is'$-pairing symmetry which belong to point (ii) above. Here, the origin of an $s + is'$ combination is interesting. Because of the s-wave nature in each band, $g_i(\mathbf{k}) = \pm 1$. There arises an internal rotational symmetry $SO(N)$ of the components of the order parameter $\Delta = \{\eta_i\}$ as, for example, $\eta_1 \to \eta_2, \eta_2 \to \eta_3, \ldots, \eta_N \to \eta_1$. Therefore, we can Fourier transform the order parameters as

$$\bar{\eta}_p = \frac{1}{\sqrt{N}} \sum_{n=0}^{N-1} \eta_n \exp\left(i \frac{2\pi p}{N} n\right), \tag{10}$$

where n runs over the number of bands and $p \in \mathbb{Z}$. Clearly, although the pairing amplitude η_i for each band is real, the Fourier component $\bar{\eta}_p$ is complex for $p \neq 0$, and breaks the TRS. The phases of the order parameter is clearly dictated by the total number of bands. For our five-band model, we have the order parameters which take the form $\bar{\eta}_1 = 1/\sqrt{5} \sum_{n=0}^{4} \eta_n \exp(i2\pi n/5)$. This multiband order parameter is consistent with the multigap behavior we observed in our experiments.

VII. CONCLUSIONS

To summarize, we have investigated $\mathrm{Re}_2\mathrm{Hf}$. Zero- and longitudinal-field μSR data reveal the presence of spontaneous static magnetic fields below T_C, confirming that time-reversal symmetry is broken in the superconducting state. Detailed theoretical work suggests the FS nesting frustration in the superconducting ground state leads to time-reversal symmetry breaking. This is an observation of frustrated multiband superconductivity. This work paves the way for further studies of many superconductors in the Re_2X family in the hunt for unconventional behavior. Apart from the local magnetic moment corresponding to the TRSB SC as observed here, such an exotic order parameter has other interesting experimental signatures [68–72], and also induces other collective [73,74] and topological excitations [75–77].

[1] M. Sigrist and K. Ueda, Rev. Mod. Phys. **63**, 239 (1991).

[2] D. J. Scalapino, E. Loh, Jr., and J. E. Hirsch, Phys. Rev. B **34**, 8190(R) (1986).

[3] T. M. Rice and K. Ueda, Phys. Rev. B **34**, 6420 (1986).

[4] J. R. Schrieffer, *Theory of Superconductivity* (W. A. Benjamin, New York, 1964).

[5] J. R. Schrieffer, X. G. Wen, and S. C. Zhang, Phys. Rev. B **39**, 11663 (1989).

[6] P. Monthoux, A. V. Balatsky, and D. Pines, Phys. Rev. Lett. **67**, 3448 (1991).

[7] D. J. Scalapino, Rev. Mod. Phys. **84**, 1383 (2012).

[8] J. C. S. Davis and D.-H. Lee, Proc. Natl. Acad. Sci. USA **110**, 17623 (2013).

[9] T. Das, R. S. Markiewicz, and A. Bansil, Adv. Phys. **63**, 151 (2014).

[10] P. Adhikary and T. Das, Phys. Rev. B **101**, 214517 (2020).

[11] T. Takimoto, T. Hotta, and K. Ueda, Phys. Rev. B **69**, 104504 (2004).

[12] P. Adhikary, S. Bandyopadhyay, T. Das, I. Dasgupta, and T. Saha-Dasgupta, Phys. Rev. B **102**, 100501(R) (2020).

[13] T. Das and K. Dolui, Phys. Rev. B **91**, 094510 (2015).

[14] T. Das, J.-X. Zhu, and M. J. Graf, Sci. Rep. **5**, 8632 (2015).

[15] H. Ikeda, M.-To Suzuki, and R. Arita, Phys. Rev. Lett. **114**, 147003 (2015).

[16] P. Adhikary and T. Das, SciPost Phys. **7**, 078 (2019).

[17] A. Bhattacharyya, D. T. Adroja, K. Panda, S. Saha, T. Das, A. J. S. Machado, O. V. Cigarroa, T. W. Grant, Z. Fisk, A. D. Hillier, and P. Manfrinetti, Phys. Rev. Lett. **122**, 147001 (2019).

[18] I. I. Mazin, D. J. Singh, M. D. Johannes, and M. H. Du, Phys. Rev. Lett. **101**, 057003 (2008).

[19] S. Graser, T. A. Maier, P. J. Hirschfeld, and D. J. Scalapino, New J. Phys. **11**, 025016 (2009).

[20] Z.-J. Yao, J.-X. Li, and Z. D. Wang, New J. Phys. **11**, 025009 (2009).

[21] A. Chubukov, Annu. Rev. Condens. Matter Phys. **3**, 57 (2012).

[22] S. Ray, J. Jung, and T. Das, Phys. Rev. B **99**, 134515 (2019).

[23] G. M. Luke, Y. Fudamoto, K. M. Kojima, M. I. Larkin, J. Merrin, B. Nachumi, Y. J. Uemura, Y. Maeno, Z. Q. Mao, Y. Mori, H. Nakamura, and M. Sigrist, Nature (London) **394**, 558 (1998).

[24] J. Xia, Y. Maeno, P. T. Beyersdorf, M. M. Fejer, and A. Kapitulnik, Phys. Rev. Lett. **97**, 167002 (2006).

[25] G. M. Luke, A. Keren, L. P. Le, W. D. Wu, Y. J. Uemura, D. A. Bonn, L. Taillefer, and J. D. Garrett, Phys. Rev. Lett. **71**, 1466 (1993).

[26] P. D. d. Reotier, A. Huxley, A. Yaouanc, J. Flouquet, P. Bonville, P. Imbert, P. Pari, P. C. M. Gubbens, and A. M. Mulders, Phys. Lett. A **205**, 239 (1995).

[27] W. Higemoto, K. Satoh, N. Nishida, A. Koda, K. Nagamine, Y. Haga, E. Yamamoto, N. Kimura, and Y. Onuki, Physica (Amsterdam) **281**, 984 (2000).

[28] R. H. Heffner, J. L. Smith, J. O. Willis, P. Birrer, C. Baines, F. N. Gygax, B. Hitti, E. Lippelt, H. R. Ott, A. Schenck, E. A. Knetsch, J. A. Mydosh, and D. E. MacLaughlin, Phys. Rev. Lett. **65**, 2816 (1990).

[29] Y. Aoki, A. Tsuchiya, T. Kanayama, S. R. Saha, H. Sugawara, H. Sato, W. Higemoto, A. Koda, K. Ohishi, K. Nishiyama, and R. Kadono, Phys. Rev. Lett. **91**, 067003 (2003).

[30] L. Shu, W. Higemoto, Y. Aoki, A. D. Hillier, K. Ohishi, K. Ishida, R. Kadono, A. Koda, O. O. Bernal, D. E. MacLaughlin, Y. Tunashima, Y. Yonezawa, S. Sanada, D. Kikuchi, H. Sato, H. Sugawara, T. U. Ito, and M. B. Maple, Phys. Rev. B **83**, 100504(R) (2011).

[31] A. Maisuradze, W. Schnelle, R. Khasanov, R. Gumeniuk, M. Nicklas, H. Rosner, A. Leithe-Jasper, Yu. Grin, A. Amato, and P. Thalmeier, Rev. B **82**, 024524 (2010).

[32] A. D. Hillier, J. Quintanilla, B. Mazidian, J. F. Annett, and R. Cywinski, Phys. Rev. Lett. **109**, 097001 (2012).

[33] E. R. Schemm, W. J. Gannon, C. M. Wishne, W. P. Halperin, and A. Kapitulnik, Science **345**, 190 (2014).

[34] A. Bhattacharyya, D. T. Adroja, J. Quintanilla, A. D. Hillier, N. Kase, A. M. Strydom, and J. Akimitsu, Phys. Rev. B **91**, 060503(R) (2015).

[35] R. P. Singh, A. D. Hillier, B. Mazidian, J. Quintanilla, J. F. Annett, D. M. Paul, G. Balakrishnan, and M. R. Lees, Phys. Rev. Lett. **112**, 107002 (2014).

[36] D. Singh, J. A. T. Barker, A. Thamizhavel, D. M. Paul, A. D. Hillier, and R. P. Singh, Phys. Rev. B **96**, 180501(R) (2017).

[37] D. Singh, K. P. Sajilesh, J. A. T. Barker, D. M. Paul, A. D. Hillier, and R. P. Singh, Phys. Rev. B **97**, 100505(R) (2018).

[38] T. Shang, G. M. Pang, C. Baines, W. B. Jiang, W. Xie, A. Wang, M. Medarde, E. Pomjakushina, M. Shi, J. Mesot, H. Q. Yuan, and T. Shiroka, Phys. Rev. B **97**, 020502(R) (2018).

[39] A. D. Hillier, J. Quintanilla, and R. Cywinski, Phys. Rev. Lett. **102**, 117007 (2009).

[40] P. K. Biswas, H. Luetkens, T. Neupert, T. Sturzer, C. Baines, G. Pascua, A. P. Schnyder, M. H. Fischer, J. Goryo, M. R. Lees, H. Maeter, F. Bruckner, H. H. Klauss, M. Nicklas, P. J. Baker, A. D. Hillier, M. Sigrist, A. Amato, and D. Johrendt, Phys. Rev. B **87**, 180503(R) (2013).

[41] D. Singh, M. S. Scheurer, A. D. Hillier, D. T. Adroja, and R. P. Singh, Phys. Rev. B **102**, 134511 (2020).

[42] P. Neha, P. K. Biswas, T. Das, and S. Patnaik, Phys. Rev. Materials **3**, 074201 (2019).

[43] A. Ribak, R. Majlin, M. H. Fischer, J. Ruhman, K. Chashka, Y. Dagan, and A. Kanigel, Sci. Adv. **6**, eaax9480 (2020).

[44] sV. Grinenko, P. Materne, R. Sarkar, H. Luetkens, K. Kihou, C. H. Lee, S. Akhmadaliev, D. V. Efremov, S.-L. Drechsler, and H.-H. Klauss, Phys. Rev. B **95**, 214511 (2017).

[45] R. L. Berry and G. V. Raynor, Acta Cryst. **6**, 178 (1953).

[46] See Supplemental Material at http://link.aps.org/supplemental/ 10.1103/PhysRevB.105.094513 for time-reversal symmetry breaking in the frustrated superconductor Re$_2$Hf.

[47] Y. Li, W. Tabis, Y. Tang, G. Yu, J. Jaroszynski, N. Barisic, and M. Greven, Sci. Adv. **5**, eaap7349 (2019).

[48] M. Tinkham, *Introduction to Superconductivity*, 2nd ed. (McGraw-Hill, New York, 1996).

[49] K. Maki, Phys. Rev. **148**, 362 (1966).

[50] E. Helfand and N. R. Werthamer, Phys. Rev. **147**, 288 (1966).

[51] N. R. Werthamer, E. Helfand, and P. C. Hohenberg, Phys. Rev. **147**, 295 (1966).

[52] W. L. McMillan, Phys. Rev. **167**, 331 (1968).

[53] M. Mandal, C. Patra, A. Kataria, D. Singh, P. K. Biswas, J. S. Lord, A. D. Hillier, and R. P. Singh, Phys. Rev. B **104**, 054509 (2021).

[54] M. Mandal, K. P. Sajilesh, R. Roy Chowdhury, D. Singh, P. K. Biswas, A. D. Hillier, and R. P. Singh, Phys. Rev. B **103**, 054501 (2021).

[55] H. Padamsee, J. E. Neighbor, and C. A. Shiffman, J. Low. Temp. Phys. **12**, 387 (1973).

[56] M. Isobe, M. Arai, and N. Shirakawa, Phys. Rev. B **93**, 054519 (2016).

[57] N. Nakai, P. Miranovic, M. Ichioka, and K. Machida, Phys. Rev. B **70**, 100503(R) (2004).

[58] K. Izawa, A. Shibata, Y. Matsuda, Y. Kato, H. Takeya, K. Hirata, C. J. van der Beek, and M. Konczykowski, Phys. Rev. Lett. **86**, 1327 (2001).

[59] H. Kim, K. Cho, M. A. Tanatar, V. Taufour, S. K. Kim, S. L. Budko, P. C. Canfield, V. G. Kogan, and R. Prozorov, Symmetry **11**, 1012 (2019).

[60] F. Bouquet, Y. Wang, I. Sheikin, T. Plackowski, A. Junod, S. Lee, and S. Tajima, Phys. Rev. Lett. **89**, 257001 (2002).

[61] C. L. Huang, J.-Y. Lin, Y. T. Chang, C. P. Sun, H. Y. Shen, C. C. Chou, H. Berger, T. K. Lee, and H. D. Yang, Phys. Rev. B **76**, 212504 (2007).

[62] R. S. Hayano, Y. J. Uemura, J. Imazato, N. Nishida, T. Yamazaki, and R. Kubo, Phys. Rev. B **20**, 850 (1979).

[63] T. Shang, M. Smidman, S. K. Ghosh, C. Baines, L. J. Chang, D. J. Gawryluk, J. A. T. Barker, R. P. Singh, D. McK. Paul, G. Balakrishnan, E. Pomjakushina, M. Shi, M. Medarde, A. D. Hillier, H. Q. Yuan, J. Quintanilla, J. Mesot, and T. Shiroka, Phys. Rev. Lett. **121**, 257002 (2018).

[64] G. Kresse and J. Furthmuller, Phys. Rev. B **54**, 11169 (1996).

[65] J. P. Perdew, K. Burke, and M. Ernzerhof, Phys. Rev. Lett. **77**, 3865 (1996).

[66] A. L. Giorgi and E. G. Szklarz, J. Less-Common Met. **22**, 246 (1970).

[67] D. F. Agterberg, V. Barzykin, and L. P. Gorkov, Phys. Rev. B **60**, 14868 (1999).

[68] V. Stanev and Z. Tesanovic, Phys. Rev. B **81**, 134522 (2010).

[69] Y. Tanaka and T. Yanagisawa, Solid State Commun. **150**, 1980 (2010).

[70] X. Hu and Z. Wang, Phys. Rev. B **85**, 064516 (2012).

[71] B. J. Wilson and M. P. Das, J. Phys.: Condens. Matter **25**, 425702 (2013).

[72] S.-Z. Lin, S. Maiti, and A. Chubukov, Phys. Rev. B **94**, 064519 (2016).

[73] V. Stanev, Phys. Rev. B **85**, 174520 (2012).

[74] S.-Z. Lin and X. Hu, Phys. Rev. Lett. **108**, 177005 (2012).

[75] J. Garaud, J. Carlstrom, E. Babaev, and M. Speight, Phys. Rev. B **87**, 014507 (2013).

[76] S. R. Elliott and M. Franz, Rev. Mod. Phys. **87**, 137 (2015).

[77] M. Sato and Y. Ando, Rep. Prog. Phys. **80**, 076501 (2017).